

# Kernel-Based Vector Field Reconstruction in Computational Fluid Dynamic Models

L. Bonaventura<sup>\*b</sup>, A. Iske<sup>‡</sup>, E. Miglio<sup>b</sup>

<sup>b</sup> *MOX – Modellistica e Calcolo Scientifico  
Dipartimento di Matematica “F. Brioschi”  
Politecnico di Milano  
Via Bonardi 9, 20133 Milano, Italy*

<sup>‡</sup> *Department of Mathematics  
University of Hamburg  
Bundesstraße 55  
D-20146 Hamburg, Germany*

## SUMMARY

Kernel-based reconstruction methods are applied to obtain highly accurate approximations of local vector fields from normal components assigned at the edges of a computational mesh. The theoretical background of kernel-based reconstructions for vector-valued functions is first reviewed, before the reconstruction method is adapted to the specific requirements of relevant applications in computational fluid dynamics. To this end, important computational aspects concerning the design of the reconstruction scheme, such as the selection of suitable stencils, are explained in detail. Extensive numerical examples and comparisons concerning hydrodynamic models show that the proposed kernel-based reconstruction improves the accuracy of standard finite element discretizations, including Raviart-Thomas (RT) elements, quite significantly, while retaining discrete conservation properties of important physical quantities, such as mass, vorticity or potential enstrophy. Copyright © 2000 John Wiley & Sons, Ltd.

## KEY WORDS:

Kernel-based approximation methods, local vector field reconstruction, Raviart-Thomas (RT) elements, computational fluid dynamics

## 1. INTRODUCTION

Kernel-based reconstruction methods have recently gained enormous popularity in relevant applications of computational science and engineering, such as meshfree discretizations for partial differential equations [11, 12, 13, 14], particle-based numerical simulations [18], machine learning [36] and manifold learning [21], as well as in many other challenging problems of *high-dimensional* approximation.

---

\*Correspondence to: MOX – Modellistica e Calcolo Scientifico, Dipartimento di Matematica “F. Brioschi”, Politecnico di Milano, Via Bonardi 9, 20133 Milano, Italy

Radial (reproducing) kernels, also referred to as *radial basis functions* (RBFs), are powerful tools for interpolation and approximation of scalar-valued multivariate functions. In fact, radial kernels provide highly accurate reconstructions from discrete scattered data without imposing too severe restrictions on the spatial distribution of the sample points. Moreover, customized preconditioners lead to stable implementations of the reconstruction scheme, whose evaluation is fast – due to the kernel’s simple representation. Therefore, radial kernels are especially very popular in applications of high-dimensional approximation. For a recent account on theoretical and practical aspects of radial (reproducing) kernels and their applications, we refer to the textbooks [7, 17, 40].

Suitable choices for radial kernels include *polyharmonic splines*, *Gaussians*, and (*inverse*) *multiquadrics*, where the latter two kernels may (for band-limited target functions) lead to spectral convergence rates of the respective interpolation methods. Moreover, it can be shown that, in this case, also any derivative of the interpolated target function can be approximated accurately by the corresponding derivative of the kernel-based interpolant, see [40, Chapter 11] for theoretical details on error bounds.

Quite recently, different concepts of meshfree methods were developed to solve numerically partial differential equations by radial kernels, where the utilized approaches include collocation methods [9, 10], Galerkin methods [39], and methods of backward characteristics [4], to mention but a few.

But the utility of radial kernels has also been shown for mesh-based methods, such as for instance in [19, 38] where radial kernels were used to obtain highly accurate finite volume ENO schemes by local reconstruction from scattered cell average values. Radial kernels were also applied to semi-Lagrangian discretizations in [3], and similar interpolation approaches based on kriging were used in [34]. In [32, 33], interpolation by radial kernels is essential to achieve accurate semi-Lagrangian schemes on Cartesian grids with cut boundary cells. Another example is the recent adaptive ADER scheme [20], where kernel-based interpolation is used to construct appropriate error estimators for mesh adaptation. Moreover, radial kernels were used in [42] to develop high order approximation schemes for discretizing differential operators of the shallow water equations.

In all these applications, *scalar-valued* radial kernels were used for local interpolation, which allows one to reconstruct a function at any point in space, given its *scalar* values in a neighbourhood of that point. In this paper, we aim at pursuing further this development by using radial kernels for the interpolation of *vector-valued* functions. In this case, due to the reconstruction scheme, the radial kernel is required to be *matrix-valued* rather than *scalar-valued*.

The overall framework of Hermite-Birkhoff interpolation via matrix-valued radial kernels is covered in outmost generality through the seminal paper [24] of Narcowich and Ward. Although we believe that the 1994 paper [24] has remarkably great potential for applications in computational fluid dynamics and related fields, it seems that it has not gained much attention in applications since then. Indeed, more *ad hoc* reconstruction approaches were developed instead, e.g. in [27, 37] for similar problems.

In the present paper, relevant theoretical details from [24] are briefly reviewed first, before some of the theory is adapted to the particular requirements of specific applications in computational fluid dynamics which we wish to address here. To this end, we will specialize the very general method of [24] to design much simpler, yet powerful, reconstruction schemes by *diagonally-scaled* radial kernels, in which case the *matrix-valued* radial kernel is given

by a diagonal matrix. This way we wish to make the results of [24] more accessible. The primary goal of this paper, however, is to provide accurate vector field reconstructions in order to improve standard finite element discretizations, such as low order Raviart-Thomas (RT) elements [28, 30].

In RT finite element methods, discrete vector fields are usually represented by their components normal to the edges of the computational mesh. Relevant applications of RT elements include electromagnetic [15] and hydrodynamical problems, the latter being the focus of the present paper.

The lowest order RT elements lead easily to numerical methods that exhibit appealing mimetic properties, such as conservation of mass, vorticity and potential enstrophy. Recent methods for computational fluid dynamics applications, such as [5, 6, 8, 23, 27], rely on the above mentioned conservation properties. In contrast, although higher order RT elements are available (see e.g. [25]), to the best of our knowledge we are not aware of any work on higher order methods (using RT or other elements) displaying such discrete preservation properties. The kernel-based Gaussian reconstruction method proposed in this paper allows us to enhance the accuracy of low order RT elements, while retaining the important discrete conservation properties of the above mentioned schemes.

The outline of this paper is as follows. In Section 2, key features of kernel-based vector field reconstruction (by using diagonally-scaled radial kernels) are first reviewed, before the specific vector reconstruction problem is explained in Section 3. Practical aspects concerning the implementation of the proposed reconstruction method are also addressed, especially the choice of suitable stencils. In Section 4, the accuracy of the utilized kernel-based Gaussian reconstruction scheme is assessed in comparison with RT elements of order zero,  $RT_0$ . This is done through specific numerical experiments, where accuracy rates are determined numerically for both methods. Finally, in Section 5, the practical relevance of the proposed kernel-based vector field reconstruction method is demonstrated by using two different shallow water models, aiming at atmospheric and coastal modelling, respectively.

## 2. VECTOR FIELD RECONSTRUCTION FROM HERMITE-BIRKHOFF DATA

This section explains kernel-based reconstruction for vector-valued functions from scattered Hermite-Birkhoff data. In order to discuss this problem, let  $u : \mathbb{R}^d \rightarrow \mathbb{R}^n$  denote a vector-valued function,  $u = (u_1, \dots, u_n)$ . Moreover, assume that for a finite set  $\Lambda = \{\lambda\}_{\lambda \in \Lambda}$  of linearly independent vector-valued linear functionals, samples  $\lambda(u) \in \mathbb{R}$  are given, where the action of any  $\lambda = (\lambda_1, \dots, \lambda_n) \in \Lambda$  on  $u$  is defined as

$$\lambda(u) = \sum_{k=1}^n \lambda_k(u_k).$$

Specific examples for functionals  $\lambda$ , as we utilize them in relevant hydrodynamical applications, are given in Section 3.

Reconstruction of  $u$  from values  $\{\lambda(u) : \lambda \in \Lambda\}$  requires finding a suitable recovery function  $s : \mathbb{R}^d \rightarrow \mathbb{R}^n$  satisfying

$$\lambda(s) = \lambda(u), \quad \text{for all } \lambda \in \Lambda, \tag{1}$$

or,  $s|_{\Lambda} = u|_{\Lambda}$ , in short hand notation. For the sake of computational efficiency, the approach

taken in this paper uses *diagonally-scaled* matrix-valued radial kernel functions. In this case, the *matrix-valued* radial kernel is given by a diagonal matrix.

In order to explain this particular reconstruction scheme more precisely, let  $\Phi : \mathbb{R}^d \rightarrow \mathbb{R}^{n \times n}$  be a diagonal matrix-valued function,

$$\Phi(\mathbf{x}) = \text{diag}(\phi_1(\mathbf{x}), \dots, \phi_n(\mathbf{x})) = \begin{bmatrix} \phi_1(\mathbf{x}) & & \\ & \ddots & \\ & & \phi_n(\mathbf{x}) \end{bmatrix} \in \mathbb{R}^{n \times n} \quad \text{for } \mathbf{x} \in \mathbb{R}^d \quad (2)$$

with scalar-valued diagonal components  $\phi_j : \mathbb{R}^d \rightarrow \mathbb{R}$ ,  $1 \leq j \leq n$ . Moreover, we assume that  $\Phi$  is *even*,  $\Phi(\mathbf{x}) = \Phi(-\mathbf{x})$  for all  $\mathbf{x} \in \mathbb{R}^d$ , i.e.,  $\phi_j(\mathbf{x}) = \phi_j(-\mathbf{x})$  for all  $1 \leq j \leq n$ . Suitable entries for the diagonal components  $\phi_j$  of  $\Phi$  in (2) are *radial* kernel functions,  $\phi(r) \equiv \phi_j(r)$ ,  $r = \|\mathbf{x}\|$ , where popular choices include Gaussians,  $\phi(r) = e^{-r^2}$ , and inverse multiquadrics,  $\phi(r) = 1/\sqrt{1+r^2}$ .

Now according to the proposed reconstruction scheme, the interpolant  $s$  in (1) is has the form

$$s = \tau * \Phi \quad \text{with } \tau = \sum_{\mu \in \Lambda} c_\mu \mu, \quad (3)$$

where the convolution product

$$\tau * \Phi : \mathbb{R}^d \rightarrow \mathbb{R}^n$$

between the diagonal matrix  $\Phi$  and the functional  $\tau = (\tau_1, \dots, \tau_n)$  is defined componentwise as

$$[\tau * \Phi]_j(\mathbf{x}) = \tau_j \phi_j(\mathbf{x} - \mathbf{y}) \quad \text{for } 1 \leq j \leq n.$$

Therefore, any component  $s_j$ ,  $1 \leq j \leq n$ , of the reconstruction  $s = (s_1, \dots, s_n)$  in (3) can be expressed as

$$s_j(\mathbf{x}) = [\tau * \Phi]_j(\mathbf{x}) = \sum_{\mu \in \Lambda} c_\mu [\mu * \Phi]_j(\mathbf{x}) = \sum_{\mu \in \Lambda} c_\mu \mu_j^{\mathbf{y}} \phi_j(\mathbf{x} - \mathbf{y}), \quad (4)$$

where  $\mu_j^{\mathbf{y}}$  denotes action of the functional  $\mu_j$  on variable  $\mathbf{y} \in \mathbb{R}^d$ .

Now solving the reconstruction problem (1) under the assumption  $s = \tau * \Phi$  for  $s$  in (3) amounts to solving the  $N$ -by- $N$  linear equation system

$$Ac = u|_{\Lambda} \quad (5)$$

with unknown  $c = (c_\mu)_{\mu \in \Lambda} \in \mathbb{R}^N$ , where

$$A = (\lambda(\mu * \Phi))_{\mu, \lambda \in \Lambda} \in \mathbb{R}^{N \times N}, \quad (6)$$

so that any component  $a_{\mu, \lambda} = \lambda(\mu * \Phi)$  of  $A$  has the form

$$a_{\mu, \lambda} = \sum_{j=1}^n \lambda_j^{\mathbf{x}} \mu_j^{\mathbf{y}} \phi_j(\mathbf{x} - \mathbf{y}) \quad \text{for } \mu, \lambda \in \Lambda.$$

Note that the linear system (5) has, for any input data, a unique solution, provided that  $\Phi$  is *positive definite*, which in other words means that the matrix  $A$  in (6) is for any combination of admissible input data – functionals  $\Lambda$  and function values  $u|_{\Lambda}$  – positive definite.

**Definition 1.** Let  $\Phi : \mathbb{R}^d \rightarrow \mathbb{R}^{n \times n}$  be an even matrix-valued function. We say that  $\Phi$  is positive definite, iff the quadratic form

$$\sum_{\mu, \lambda \in \Lambda} c_\mu c_\lambda \lambda(\mu * \Phi) \tag{7}$$

is positive for any set  $\Lambda = \{\lambda\}_{\lambda \in \Lambda}$  of linearly independent functionals and any non-zero vector  $c = (c_\mu) \in \mathbb{R}^N \setminus \{0\}$ .

The class of positive definite matrix-valued functions will be denoted in the following by **PD**. It is straightforward to show that any diagonal matrix-valued function  $\Phi$  is positive definite, if and only if all its diagonal components  $\phi_j$ ,  $1 \leq j \leq n$ , are positive definite. We prove this simple but quite useful characterization later in this section through Lemma ???. To this end, let us first make some further preparations. Note that the Definition 1 for positive definite vector-valued functions covers in particular the special case of scalar-valued functions, where  $n = 1$ . Therefore, it makes sense to require  $\phi_j \in \mathbf{PD}$  for the individual scalar-valued components of  $\Phi$  in (2).

But scalar-valued positive definite functions are well-understood. Moreover, the class of radial positive definite functions can be characterized through *completely monotone functions* [22]. This particular characterization – due to I.J. Schoenberg in 1938 – gives a useful necessary and sufficient criterion for the construction of radial positive definite kernel functions. For details, we refer to [22]. Important examples for scalar-valued radial positive definite functions, *radial kernels*,  $\phi \in \mathbf{PD}$ , are Gaussians,  $\phi(r) = e^{-r^2}$ , and inverse multiquadrics,  $\phi(r) = 1/\sqrt{1+r^2}$ , as already mentioned at the outset of this section.

We further remark that the class of positive definite functions is *scale-invariant*, so that in particular both  $\phi(r) = e^{-\alpha r^2} \in \mathbf{PD}$  and  $\phi(r) = 1/\sqrt{\alpha^2 + r^2} \in \mathbf{PD}$  are positive definite for any scalar  $\alpha > 0$ . In fact, this observation is of crucial importance in the numerical experiments of Sections 4 and 5.

Another important observation is concerning the well-posedness of the utilized reconstruction scheme: if all  $n$  scalar-valued diagonal components  $\phi_j$ ,  $1 \leq j \leq n$ , of  $\Phi = \text{diag}(\phi_1, \dots, \phi_n)$  are positive definite, then  $\Phi$  is positive definite. Indeed, this is due the representation

$$\begin{aligned} \sum_{\mu, \lambda \in \Lambda} c_\mu c_\lambda \lambda(\mu * \Phi) &= \sum_{\mu, \lambda \in \Lambda} c_\mu c_\lambda \sum_{j=1}^n \lambda_j^x(\mu_j^y \phi_j(\mathbf{x} - \mathbf{y})) \\ &= \sum_{j=1}^n \left[ \sum_{\mu, \lambda \in \Lambda} c_\mu c_\lambda \lambda_j^x(\mu_j^y \phi_j(\mathbf{x} - \mathbf{y})) \right] \end{aligned} \tag{8}$$

for the quadratic form in (7), which is in this case positive for any  $c \in \mathbb{R}^N \setminus \{0\}$ , i.e.,  $\Phi$  is positive definite. Note that the converse is also true, i.e., if  $\Phi = \text{diag}(\phi_1, \dots, \phi_n)$  is positive definite, then all  $\phi_j$ ,  $1 \leq j \leq n$ , must be positive definite.

Let us finally remark that the reconstruction scheme of this section can be generalized from *positive definite*  $\Phi \in \mathbf{PD}$  to *conditionally positive definite*  $\Phi$ , by following along the lines of Narcowich and Ward [24]. This would lead to a larger family of potentially available  $\phi_j$ , albeit with a more complicated reconstruction scheme. We omit further technical aspects, since these lengthy details are clearly beyond the aims and scope of this paper. For the sake of computational efficiency, we rather prefer to work with positive definite radial kernels  $\Phi \in \mathbf{PD}$ .

Let us conclude the discussion of this section as follows.

**Theorem 1.** *Let  $\Phi = \text{diag}(\phi_1, \dots, \phi_n)$  be positive definite,  $\Phi \in \mathbf{PD}$ , i.e.  $\phi_j \in \mathbf{PD}$  for all  $1 \leq j \leq n$ . Then the reconstruction problem (1) has a unique solution  $s$  of the form*

$$s(\mathbf{x}) = \sum_{\mu \in \Lambda} c_\mu (\mu * \Phi)(\mathbf{x}),$$

where the coefficients  $c = (c_\mu)_{\mu \in \Lambda}$  of  $s$  can be computed by solving the linear system  $Ac = u|_\Lambda$ , whose coefficient matrix  $A$  in (6) is positive definite. Any component  $s_j$  of  $s = (s_1, \dots, s_n)$  can be expressed as

$$s_j(\mathbf{x}) = \sum_{\mu \in \Lambda} c_\mu \mu_j^y \phi_j(\mathbf{x} - \mathbf{y}) \quad \text{for } 1 \leq j \leq n.$$

■

Concrete and relevant examples for  $s$ ,  $\Phi$  and  $\Lambda$  are given in the following two sections.

### 3. LOCAL VECTOR FIELD RECONSTRUCTION IN TWO DIMENSIONS

We now formulate the specific vector reconstruction problem that we wish to address in hydrodynamical applications, some of which are discussed in Section 5. In this particular case we work with planar vector fields  $u : \mathbb{R}^2 \rightarrow \mathbb{R}^2$ ,  $u = [u_1, u_2]$ , so that  $d = 2$  and  $n = 2$ . Moreover, we assume we are given a (possibly scattered) set  $\mathbf{X} = \{\mathbf{x}_1, \dots, \mathbf{x}_N\} \subset \mathbb{R}^2$  of  $N$  pairwise distinct planar points, where each  $\mathbf{x}_i \in \mathbf{X}$  corresponds to a unit vector  $\mathbf{n}_i^T = [n_i^1, n_i^2] \in \mathbb{R}^2$ , satisfying  $\|\mathbf{n}_i\| = 1$ , for  $1 \leq i \leq N$ .

Now we wish to reconstruct a smooth vector field  $u : \mathbb{R}^2 \rightarrow \mathbb{R}^2$ , from given scalar samples  $u_i = \mathbf{n}_i^T \cdot u(\mathbf{x}_i) \in \mathbb{R}$ , for  $1 \leq i \leq N$ . According to the reconstruction scheme proposed in the previous section, we are concerned with solving

$$\lambda_i(u) = \lambda_i(s), \quad \text{for } 1 \leq i \leq N,$$

where  $\lambda_i = \mathbf{n}_i^T \cdot \delta_{\mathbf{x}_i}$ , and where  $\delta_{\mathbf{x}_i}$  denotes the Dirac point evaluation functional, defined as  $\delta_{\mathbf{x}_i}(u) = u(\mathbf{x}_i) \in \mathbb{R}^2$ , for  $1 \leq i \leq N$ .

Recall that the recovery function  $s = (s_1, s_2) : \mathbb{R}^2 \rightarrow \mathbb{R}^2$  is required to have the form (3), and whose two components can be expressed as in (4). Moreover, we assume

$$\Phi = \text{diag}(\phi_1, \phi_2) = \begin{bmatrix} \phi_1 & 0 \\ 0 & \phi_2 \end{bmatrix}.$$

Hence,  $\lambda_i * \Phi$ ,  $1 \leq i \leq N$ , has the form

$$(\lambda_i * \Phi)(\mathbf{x}) = \begin{bmatrix} \phi_1(\mathbf{x} - \mathbf{x}_i)n_i^1 \\ \phi_2(\mathbf{x} - \mathbf{x}_i)n_i^2 \end{bmatrix}, \quad \text{for } 1 \leq i \leq N, \quad (9)$$

and therefore, the reconstruction  $s$  in (3) can be expressed as

$$s(\mathbf{x}) = \sum_{i=1}^N c_i \begin{bmatrix} \phi_1(\mathbf{x} - \mathbf{x}_i)n_i^1 \\ \phi_2(\mathbf{x} - \mathbf{x}_i)n_i^2 \end{bmatrix}.$$

Moreover, the unknown coefficients  $c = (c_1, \dots, c_N)^T \in \mathbb{R}^N$  of  $s$  are computed by solving the linear system  $Ac = u|_\Lambda$  in (5), where

$$u|_\Lambda = (\lambda_1(u), \dots, \lambda_N(u))^T = (\mathbf{n}_1^T u(\mathbf{x}_1), \dots, \mathbf{n}_N^T u(\mathbf{x}_N))^T \in \mathbb{R}^N,$$

and where the entries in the positive definite matrix  $A = (a_{ij})_{1 \leq i, j \leq N} \in \mathbb{R}^{N \times N}$  are given by

$$a_{ij} = \lambda_j(\lambda_i * \Phi) = n_j^1 n_i^1 \phi_1(\mathbf{x}_j - \mathbf{x}_i) + n_j^2 n_i^2 \phi_2(\mathbf{x}_j - \mathbf{x}_i), \quad \text{for } 1 \leq i, j \leq N.$$

#### 4. COMPARISONS BETWEEN GAUSSIAN KERNELS AND RT ELEMENTS

In this section, we present selected numerical experiments in order to assess the *effective* accuracy order of kernel-based reconstruction by using the positive definite Gaussians, where we let  $\phi_1(r) \equiv \phi_2(r) \equiv \phi(r) = e^{-r^2 \alpha} \in \mathbf{PD}$ . According to available theoretical bounds [40, Chapter 11], spectral convergence rates can be proven for a very small class of smooth functions. But for hydrodynamic models from realistic application scenarios (in particular for the shallow water models in Section 5) we rely on less smoothness, so that the theoretical error bounds do no longer apply.

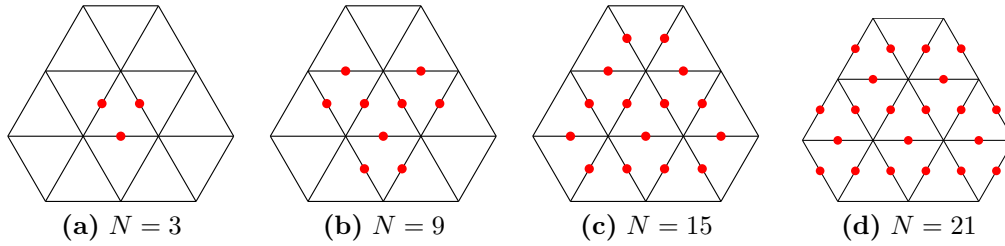
The scaling parameter  $\alpha$  in the radial kernel, was chosen in general according to the suggestion in [32], e.g. by assigning to it a value of the same order of magnitude as the size of the computational domain. This choice only relies on heuristic arguments and not on a rigorous analysis. On the other hand, it has proven to be effective in a number of applications, see e.g. [32, 33]. We have checked that changing the scale value to others of the same order of magnitude did not apparently affect the results. This choice is however a key point in the application of radial kernels and should be investigated in greater depth.

Moreover, we remark that the spectral condition number  $\kappa(A)$  of the arising interpolation matrix  $A$  is large, if the minimal distance between different sample points is small. To further explain this, if two sample points are (nearly) coincident, then two rows (columns) of the matrix  $A$  are (nearly) coincident. In this case, the conditioning of the corresponding linear system is from a numerical viewpoint very critical – due to a large condition number  $\kappa(A)$ .

In order to achieve a reasonable trade-off between the numerical stability of the proposed reconstruction scheme, on the one hand, and its resulting accuracy, on the other hand, we work with sets of interpolation points, stencils, lying on a hexagonal grid, as shown in Figure 1. In this case, the interpolation points of the stencils are well-separated, i.e., small distances between the interpolation points are avoided. Our numerical results concerning Gaussian reconstruction, as reflected by Tables I and II, are involving four different stencils of sizes  $N = 3, 9, 15, 21$ , see Figure 1. For further motivation concerning this particular point sampling we refer to our previous findings in [17, Subsection 3.9].

To evaluate the methods' approximation behaviour, we consider the resulting maximal error  $\epsilon = \|s - u\|_\infty$  among the barycenters of the triangles in the stencils' corresponding Delaunay triangulation, see Figure 1. Similar to the assessment in our previous paper [32] concerning kernel-based reconstruction for the scalar case, we consider using the vector field

$$\begin{bmatrix} u \\ v \end{bmatrix} = \begin{bmatrix} \cos(k \pi (x - \frac{1}{4})) \sin(k \pi (y - \frac{1}{4})) \\ \sin(k \pi (x - \frac{1}{4})) \cos(k \pi (y - \frac{1}{4})) \end{bmatrix},$$

Figure 1. Stencils of different sizes  $N$  for accuracy tests.

where increasingly denser data sets are used. The data sets were generated by scaling the interpolation points  $\mathbf{X}$ , so that  $q_{\mathbf{X}} \equiv h = 2^{-i}$ ,  $i = 0, 1, 2, 3, 4$ , for the *separation distance*

$$q_{\mathbf{X}} = \min_{\substack{\mathbf{x}, \mathbf{y} \in \mathbf{X} \\ \mathbf{x} \neq \mathbf{y}}} \|\mathbf{x} - \mathbf{y}\|$$

of the interpolation points in stencil  $\mathbf{X}$ .

The numerical results in Table I show the approximation error  $\epsilon(\text{RT}_0)$  obtained when using Raviart-Thomas elements of order zero,  $\text{RT}_0$ , in comparison with the approximation error  $\epsilon(\text{RBF})$  of Gaussian reconstruction. Table I also shows the corresponding spectral condition number  $\kappa(A)$  of the Gaussian interpolation matrix  $A$ . For the purpose of further comparison, corresponding approximation errors obtained with a  $\text{RT}_1$  reconstruction are also shown, along with estimates for the resulting convergence rates. The test were performed for a decreasing sequence of separation distances  $h = 2^{-i}$ ,  $i = 0, 1, 2, 3, 4$ , just before the linear system of Gaussian reconstruction becomes numerically unstable, due to too large spectral condition numbers, cf. the last column of Table I.

Table I. Comparison between  $\text{RT}_0$ ,  $\text{RT}_1$  and Gaussian reconstruction for the 15-point stencil in Figure 1 (c). The relative approximation error  $\epsilon$ , approximate convergence rate, and spectral condition number  $\kappa(A)$  of the corresponding Gaussian interpolation matrix  $A$  are shown, respectively.

$h$	$\epsilon(\text{RT}_0)$	rate	$\epsilon(\text{RT}_1)$	rate	$\epsilon(\text{RBF})$	rate	$\kappa(A)$
$2^{-0}$	$7.177 \cdot 10^{-1}$	-	$7.0920 \cdot 10^{-1}$	-	$7.248 \cdot 10^{-1}$	-	$3.625 \cdot 10^4$
$2^{-1}$	$3.070 \cdot 10^{-1}$	1.225	$1.6431 \cdot 10^{-1}$	2.109	$1.151 \cdot 10^{-1}$	2.654	$2.511 \cdot 10^6$
$2^{-2}$	$1.349 \cdot 10^{-1}$	1.187	$4.4320 \cdot 10^{-2}$	1.890	$1.451 \cdot 10^{-2}$	2.988	$1.650 \cdot 10^8$
$2^{-3}$	$6.238 \cdot 10^{-2}$	1.112	$1.1277 \cdot 10^{-2}$	1.974	$1.773 \cdot 10^{-3}$	3.033	$1.064 \cdot 10^{10}$
$2^{-4}$	$2.991 \cdot 10^{-2}$	1.060	$2.6904 \cdot 10^{-3}$	2.067	$2.178 \cdot 10^{-4}$	3.025	$6.833 \cdot 10^{11}$

For the numerical results in Table I, the 15-point stencil of Figure 1 (c) was utilized. As expected, we obtain linear convergence for Raviart-Thomas reconstruction of order zero, whereas Gaussian reconstruction yields third order accuracy, see Table I. Moreover, despite

the small separation distance of up to  $h = 2^{-4}$ , Gaussian reconstruction is very robust. But for smaller values of  $h$ , the corresponding linear system is ill-conditioned, so that it does not make sense to further evaluate the method's accuracy.

In a second test case, we compare the approximation quality of Gaussian reconstruction for four different stencils of sizes  $N = 3, 9, 15, 21$ , displayed in Figure 1. Our numerical results are reflected by Table II (for  $N = 3, 9, 21$ ) and Table I (for  $N = 15$ ).

Table II. Gaussian reconstruction for stencils of different sizes  $N$ , see Figure 1.

$h$	$\epsilon (N = 3)$	rate	$\epsilon (N = 9)$	rate	$\epsilon (N = 21)$	rate
$2^{-0}$	$7.177 \cdot 10^{-1}$	-	$7.156 \cdot 10^{-1}$	-	$7.180 \cdot 10^{-1}$	-
$2^{-1}$	$3.070 \cdot 10^{-1}$	1.225	$1.251 \cdot 10^{-1}$	2.516	$8.767 \cdot 10^{-2}$	3.034
$2^{-2}$	$1.349 \cdot 10^{-1}$	1.187	$1.769 \cdot 10^{-2}$	2.823	$1.181 \cdot 10^{-2}$	2.892
$2^{-3}$	$6.238 \cdot 10^{-2}$	1.112	$2.594 \cdot 10^{-3}$	2.770	$1.819 \cdot 10^{-3}$	2.698
$2^{-4}$	$2.991 \cdot 10^{-2}$	1.060	$4.270 \cdot 10^{-4}$	2.603	$9.958 \cdot 10^{-5}$	4.192

Not too surprisingly, the accuracy order is increasing with the size  $N$  of the utilized stencils, see Table I and II. Indeed, the stencil with  $N = 21$  interpolation points yields the best accuracy rate among the four stencils, namely slightly above order four, whereas the stencil with  $N = 3$  points yields first order accuracy only. Indeed, for  $N = 3$  the errors differ from those of the  $RT_0$  reconstruction in the last decimal digits and the empirical convergence rates achieved by the two approaches are identical. Although no theoretical explanation is available for this fact, we think it shows that, for a smooth vector field, if only 3 normal components are provided as input, the contribution of nonlinear terms in the RBF reconstruction is marginal. We can conclude that, in the tests we performed, for any stencil with more than three interpolation points, Gaussian reconstruction is superior to  $RT_0$  reconstruction. Further numerical results supporting this statement were reported in [2].

## 5. APPLICATION TO FLUID DYNAMICS PROBLEMS

In this section, we discuss applications of the proposed kernel-based Gaussian reconstruction method to computational fluid dynamics models. More specifically, we will refer to models for the shallow water equations, using discretization approaches in which the velocity field is represented by its normal components with respect to the mesh edges. The shallow water equations model the two dimensional flow of a thin fluid layer in domains whose characteristic length in the horizontal is much larger than the fluid depth. The shallow water equations result from the Navier-Stokes equations when the hydrostatic assumption holds and only barotropic and adiabatic motions are considered. Furthermore, a vertical average is performed, so that only mean values for the velocities in the horizontal directions are considered, see e.g. [26].

The shallow water equations can be written as

$$\frac{\partial h}{\partial t} + \nabla \cdot (H\mathbf{v}) = 0, \quad (10)$$

$$\frac{\partial \mathbf{v}}{\partial t} + (\mathbf{v} \cdot \nabla)\mathbf{v} = -f\mathbf{k} \times \mathbf{v} - g\nabla h. \quad (11)$$

Here,  $\mathbf{v}$  denotes the two-dimensional velocity vector,  $\mathbf{k}$  is the radial unit vector perpendicular to the plane on which  $\mathbf{v}$  is defined (or to the local tangent plane, in case of applications in spherical geometry),  $h$  is the height of the fluid layer above a reference level,  $H = h - h_s$  is the thickness of the fluid layer,  $h_s$  is the orographic or bathymetric profile,  $g$  is the gravitational constant, and  $f$  is the Coriolis parameter. Equations (10)-(11) are the starting point for Eulerian-Lagrangian discretizations.

Another widely used formulation for applications to large scale atmospheric dynamics is the so called *vector invariant form*, see e.g. [41], which can be written as

$$\frac{\partial \mathbf{v}}{\partial t} = -(\zeta + f)\mathbf{k} \times \mathbf{v} - \nabla (gh + K). \quad (12)$$

Here,  $\zeta$  is the component of relative vorticity in the direction of  $\mathbf{k}$  and  $K = \|\mathbf{v}\|^2/2$  denotes the kinetic energy. This formulation is usually the starting point for the derivation of energy, potential enstrophy and potential vorticity preserving discretizations, see e.g. [1, 31].

Spatial discretizations with staggered arrangements of the discrete variables are popular for the shallow water equations, since they allow for better representation of the gravity wave propagation, see e.g. [29]. On unstructured grid, an analog of a staggered discretization is given by the zero order Raviart-Thomas elements  $RT_0$ , see e.g. [28]. Although high order RT elements are also available, the low order ones,  $RT_0$  elements, lead more easily to numerical methods that exhibit important discrete conservation properties, such as discrete mass or vorticity preservation. These properties are important for a number of applications and various methods which take advantage of them are discussed in the two following subsections. Our main point is that the accuracy of these models has been limited so far by the first order convergence of the  $RT_0$  elements. As it will be shown in the following, the proposed kernel-based Gaussian reconstruction can effectively improve these methods, by achieving a more accurate discretization of the nonlinear momentum advection terms, either in Eulerian or in semi-Lagrangian formulations. Although in general this is not sufficient to raise the convergence order of the overall methods, models employing kernel-based reconstructions display significantly smaller errors and have in general less numerical dissipation, making their use attractive for a number of applications.

### 5.1. EULERIAN SHALLOW WATER MODELS

Eulerian discretizations of equations (10)-(12) have been proposed in [5, 6], which preserve discrete approximations of mass, vorticity and potential enstrophy. These properties are important for numerical models of general atmospheric circulation, especially for applications to climate modelling. The two time level, semi-implicit scheme in these papers used RT reconstruction to compute the nonlinear terms in the discretization of (12). Here, we will compare results obtained with a three-time level, semi-implicit time discretization, coupled

to the potential enstrophy preserving spatial discretization of [6], using either the Raviart-Thomas algorithm or a kernel-based reconstruction of the velocity field necessary for the solution of equation (12). For these tests, we employed Gaussian reconstruction by using the positive definite Gaussian kernel  $\phi(r) = e^{-\alpha r^2}$ . Moreover, a 9-point stencil was employed, see Figure 1 (b), using the normal components to the edges of the triangle on which the interpolation is being carried out and to the edges of its nearest neighbours (i.e., of the triangles which have common edges with it). We remark that in this case the velocity components are lying on planes tangent to the sphere at the edge points where the velocity component is defined. In order to apply Gaussian reconstruction, these vector components are interpreted as vectors in three dimensional space and the procedure described in Section 3 is extended in the natural way to the three dimensional case.

We consider one stationary and two non-stationary test cases for the shallow water equations belonging to the set of standard benchmark problems introduced in [41]. First, we study how the algorithm performs when applied to test case 3 of this test suite, which consists of a steady-state, zonal geostrophic flow with a narrow jet at midlatitudes. For this test case, an analytic solution is available, so that errors can be computed by applying the numerical method at different resolutions. The values of the relative error in various norms, as computed at day 2 with different spatial resolutions and with time step  $\Delta t = 1800$  s, is displayed in Tables III and IV for both Raviart Thomas elements and Gaussian reconstruction, respectively. The convergence rates remain essentially the same, due to the fact that the second order discretization of the geopotential gradient is the same in both tests. However, it can be observed that the errors (both in the height and velocity fields) have decreased by an amount that ranges between 30 % and 50 %.

Table III. Relative errors for nonlinear terms in shallow water test case 3 obtained by using RT0 reconstruction.

Level	$\ell_2$ -error, $h$	$\ell_2$ -error, $\mathbf{v}$	$\ell_\infty$ -error, $h$	$\ell_\infty$ -error, $\mathbf{v}$
3	7.42e-3	0.25	2.53e-2	0.33
4	1.94e-3	5.9e-2	8.1e-3	9.1e-2
5	6.05e-4	1.27e-2	2.9e-3	1.87e-2
6	2.54e-4	3.19e-3	1.24e-3	4.17e-3

Table IV. Relative errors for nonlinear terms in shallow water test case 3 obtained by Gaussian reconstruction on a 9-point stencil, see Figure 1 (b).

Level	$\ell_2$ -error, $h$	$\ell_2$ -error, $\mathbf{v}$	$\ell_\infty$ -error, $h$	$\ell_\infty$ -error, $\mathbf{v}$
3	7.27e-3	0.16	2.08e-2	0.17
4	1.52e-3	3.38e-2	6.74e-3	5.77e-2
5	4.05e-4	7.7e-3	1.7e-3	1.22e-2
6	1.45e-4	2.11e-3	4.8e-4	2.89e-3

We have then considered the non-stationary test case 5 of [41], for which the initial datum consists of a zonal flow impinging on an isolated mountain of conical shape. The imbalance in

the initial datum leads to the development of a wave propagating all around the globe. This test is relevant to understand the response of the numerical model to orographic forcing. Plots of the meridional velocity component at simulation day 5 are shown in Figure 2, as computed using a timestep  $\Delta t = 900$  s on an icosahedral grid at spatial resolution of approximately 240 km. We observe that the meridional velocity field obtained by using  $RT_0$  finite elements is much less regular than that obtained by Gaussian reconstruction, which is consistent with our numerical results obtained in reference simulations at higher resolution with spectral models.

Finally, we have considered the non-stationary test case 6 of [41], for which the initial datum consists of a Rossby-Haurwitz wave of wavenumber 4. This type of wave is an analytic solution for the barotropic vorticity equation, which can also be used to test shallow water models on a time scale of up to 10-15 days. The relative vorticity field is shown in Figure 3, as computed at day 5 with a timestep of  $\Delta t = 900$  s on an icosahedral grid with a spatial resolution of approximately 240 km. It can be observed that, when using  $RT_0$  reconstruction, the structure of some vorticity extrema is disrupted, while spurious maxima and minima appear close to the poles. This is in contrast to the more regular field obtained by Gaussian reconstruction, which is in better agreement with high resolution reference simulations obtained with spectral models. Furthermore, the relative change in total energy for both model runs is displayed in Figure 4. It can be observed that total energy loss is reduced by approximately 30 % when using Gaussian reconstruction, thus reducing the numerical diffusion and improving the energy conservation properties of the model, which conserves potential enstrophy but not energy, as discussed in [6]. We remark that, for Eulerian models, the additional computational cost required by Gaussian reconstruction can be significantly reduced. Indeed, it is possible to compute for each grid cell a set of time independent coefficients that yield the velocity vector at the cell center as linear combination of the velocity components at the points included in the RBF stencil. For the model runs described above, it was observed that Gaussian reconstruction increases the required CPU time by approximately 20 % in comparison to the simpler scheme  $RT_0$ .

## 5.2. EULERIAN-LAGRANGIAN SHALLOW WATER MODELS

Numerical methods for the shallow water equations using formulation (10)-(11) have been proposed in [8, 23], which couple a mass conservative, semi-implicit discretization on unstructured Delaunay meshes to an Eulerian-Lagrangian treatment of momentum advection. The resulting methods are highly efficient due to their rather weak stability restrictions, while mass conservation allows for their practical (and successful) application to a number of pollutant and sediment transport problems. A key step of the Eulerian-Lagrangian method is the interpolation at the foot of characteristic lines. In the papers quoted above, this is performed by  $RT_0$  elements or by low order interpolation procedures based on area weighted averaging. These interpolators have at most first order convergence rate and can introduce large amounts of numerical diffusion, which limits their applicability especially in long term simulations.

Firstly, the test proposed in [42] has been carried out, in which a 800 m long and 800 m wide basin was considered. The domain was discretized by an unstructured triangular mesh with 26,812 elements and 13,868 nodes, corresponding to a horizontal resolution of approximately 2 km. The basin depth was taken to be 20 m. At the inflow boundary, a Dirichlet condition was imposed on the free surface, given by a sinusoidal wave with an amplitude of 1 m and a period of approximately 12 h and the initial velocity field was assumed to be zero. The resulting

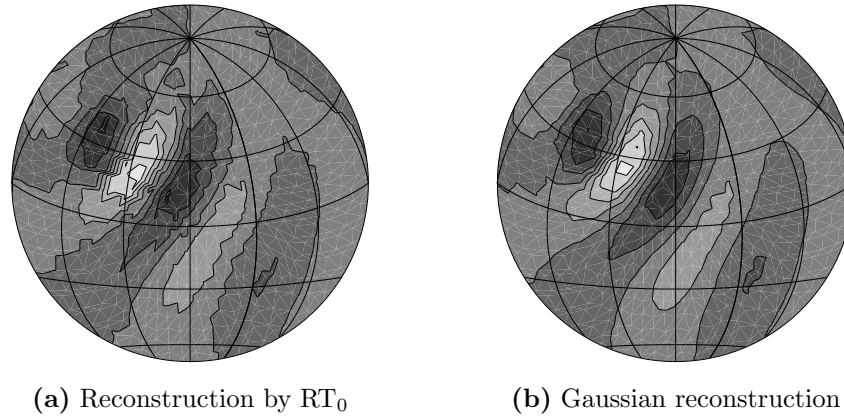
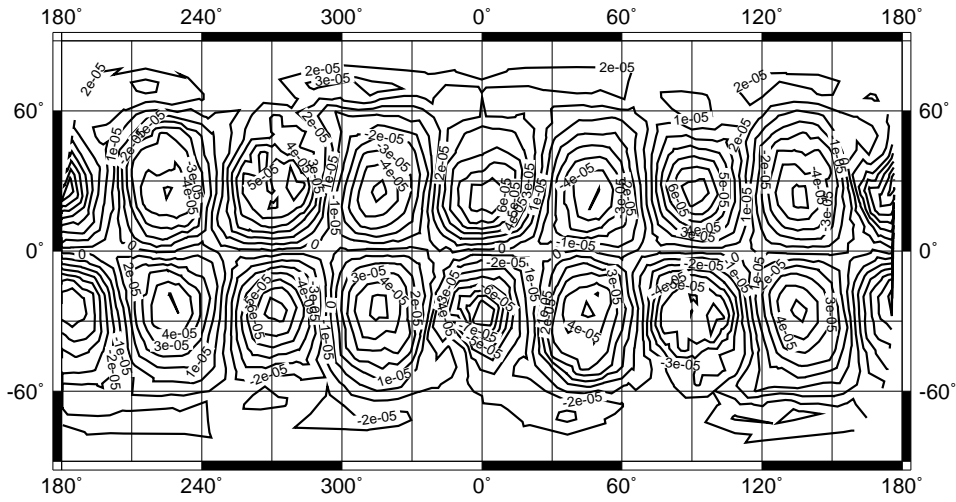
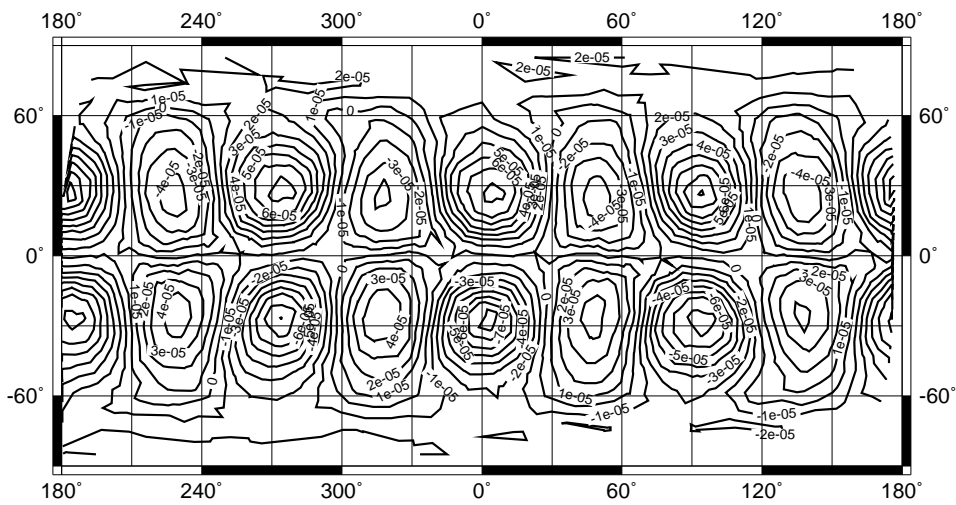


Figure 2. Meridional velocity in shallow water test case 5, obtained by (a)  $RT_0$  reconstruction (b) Gaussian reconstruction on a 9-point stencil. The contour line spacing is  $6 \text{ ms}^{-1}$ . Maximum and minimum values are approximately  $\pm 28 \text{ ms}^{-1}$ , respectively.

wavefront, computed after approximately 30 h by the Eulerian-Lagrangian method of [23], using a timestep  $\Delta t = 6 \text{ s}$  and either  $RT_0$  elements or Gaussian reconstruction at the foot of the characteristic, is displayed in Figure 5. It can be observed that for Gaussian reconstruction the wavefront is much sharper. The maximum in the free surface elevation (which would be equal to the maximum boundary value in the linear regime) is better captured by approximately 10 %. This can lead to significant improvements in a number of relevant applications, such as flooding prediction in the Venice Lagoon, which is at end of a closed sea basin of approximately the same magnitude as the simulated channel.

Furthermore, another shallow water test involving a closed rectangular basin, 150 m long and 15 m wide, was performed, whose discretization is given by an unstructured triangular mesh with 3,646 elements and 1,984 nodes. For the free surface, an unbalanced initial datum was assumed, given by  $\eta(x) = h_0 \cos(x\pi/150)$ . The amplitude of the disturbance was taken to be equal to  $h_0 = 0.1$  and the initial velocity field was assumed to be zero. The resulting free oscillations have been simulated by the same method described above, using either  $RT_0$  elements or Gaussian reconstruction at the foot of the characteristic. The free oscillations of the fluid were simulated for a total of 100 s with a timestep  $\Delta t = 0.1 \text{ s}$ . The time evolution of kinetic energy is shown in Figure 6, while the height field values computed throughout the simulation in an element close to one of the boundaries are shown in Figure 7. It can be observed that the energy dissipation caused by the interpolation of the Eulerian-Lagrangian method is reduced by 20 % when using Gaussian reconstruction, whereas the maxima and minima in the height field are improved by approximately 10 %.

In other tests, even larger improvements were observed. For example, a square domain of width 20 m was considered, which was discretized by an unstructured triangular mesh with 3,984 elements and 2,073 nodes. A constant basin depth of 2 m was assumed. At initial time, still water was assumed and the free surface profile was taken to be a Gaussian hill

(a) Reconstruction by  $RT_0$ 

(b) Gaussian reconstruction

Figure 3. Relative vorticity in shallow water test case 6, obtained by (a)  $RT_0$  reconstruction (b) Gaussian reconstruction on a 9-point stencil. The contour line spacing is  $10^{-5} \text{ ms}^{-1}$ .

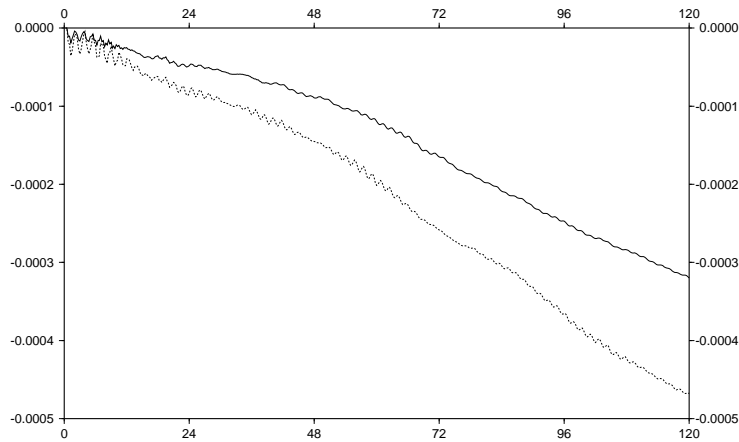


Figure 4. Relative decay in total energy in shallow water test case 6, obtained by  $RT_0$  reconstruction (dotted line) and by Gaussian reconstruction on a 9-point stencil (solid line).

centered at the center of the domain, with amplitude 0.1 m and standard deviation 2 m. In absence of any explicit dissipative term, the total energy of the system should be conserved. The free oscillations of the fluid were simulated for a total of 6 s with a timestep  $\Delta t = 0.01$  s. The time evolution of total energy is shown in Figure 8. It can be observed that the energy dissipation caused by the interpolation of the Eulerian-Lagrangian method is reduced by 40 % when using Gaussian reconstruction.

We remark that in the case of Eulerian-Lagrangian models the extra computational cost due to the use of Gaussian reconstruction is higher than in the Eulerian case. This is because the coefficients which yield the velocity vector at the cell center as linear combination of the velocity components have to be recomputed at each time step for each of the trajectory departure points.

## 6. CONCLUSIONS

The utility of diagonally-scaled radial kernel functions for accurate reconstruction of vector fields in fluid dynamics problems has been demonstrated. The theory of the utilized reconstruction method has been reviewed and adapted to applications in computational fluid dynamics. Important computational aspects concerning the implementation of the kernel-based Gaussian reconstruction method were discussed. As an example of the advantages of the proposed techniques, some applications to the discretization of the shallow water equations have been presented. Many numerical methods for these equations already exist (see e.g. among many others [], []), some of which can achieve much higher order convergence and employ more coherent treatment of all the different terms in the equations. However, we believe that our

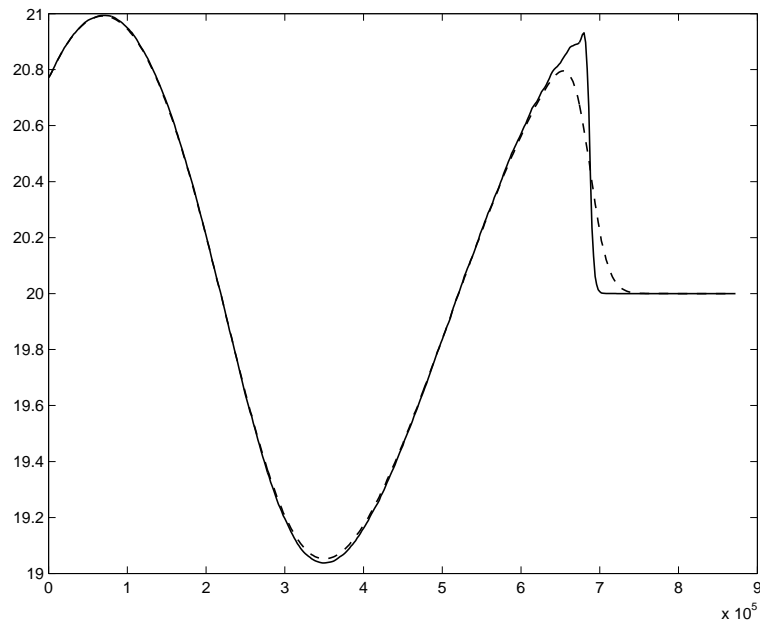


Figure 5. Free surface elevation in long channel test, obtained from  $RT_0$  reconstruction (dotted line) and Gaussian reconstruction on a 9-point stencil (solid line).

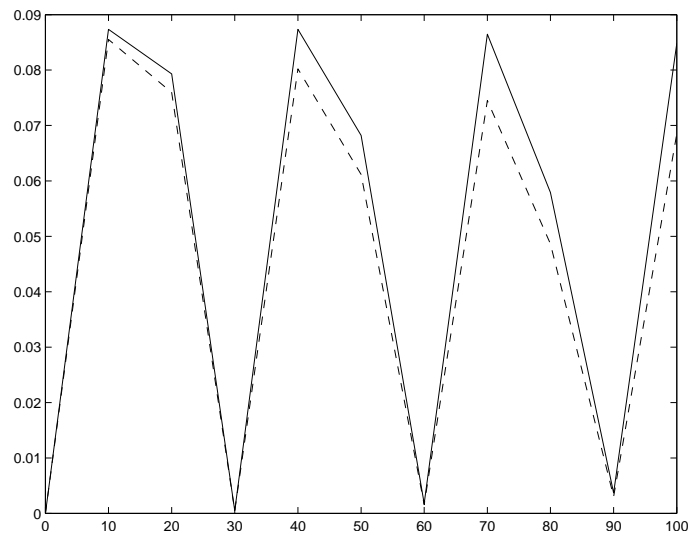


Figure 6. Kinetic energy for free oscillations test with Eulerian-Lagrangian model, obtained by  $RT_0$  reconstruction (dotted line) and Gaussian reconstruction on a 9-point stencil (solid line).

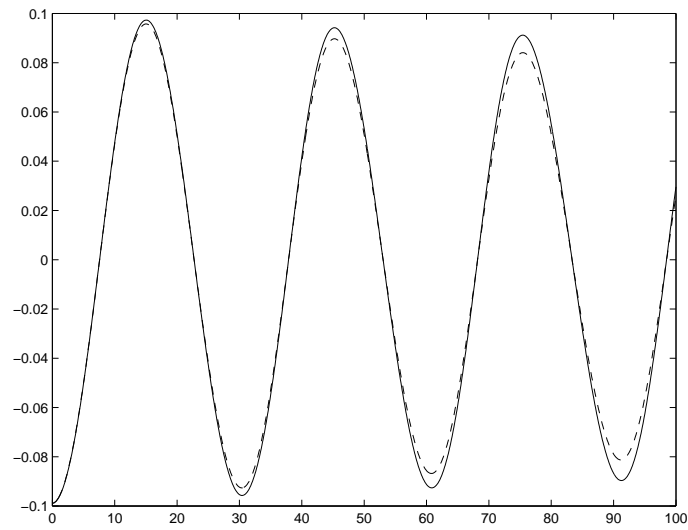


Figure 7. Height field time series at boundary element for free oscillations test with Eulerian-Lagrangian model, obtained by  $RT_0$  reconstruction (dotted line) and Gaussian reconstruction on a 9-point stencil (solid line).

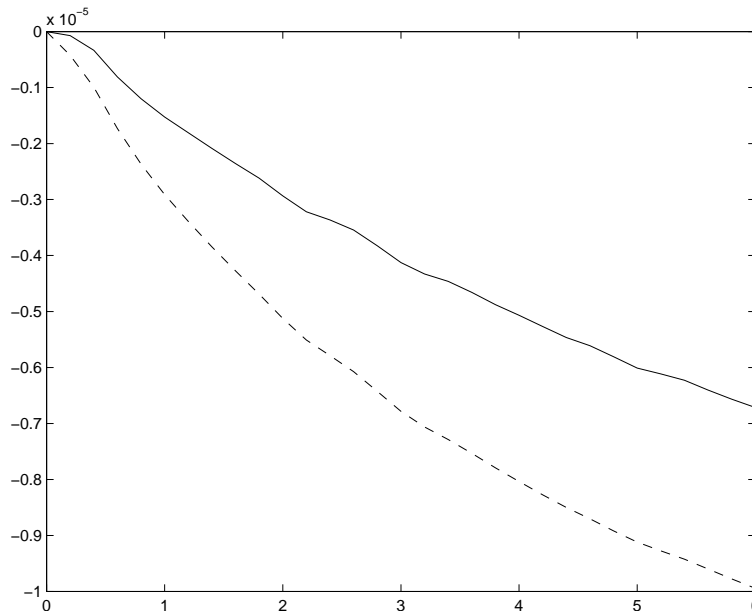


Figure 8. Relative change in total energy for free oscillations test with Eulerian-Lagrangian model, obtained by  $RT_0$  (dotted line) and Gaussian reconstruction on a 9-point stencil (solid line).

results prove that the use of radial kernel functions to improve the accuracy of low order Raviart-Thomas elements  $RT_0$  yields a convenient compromise between higher order methods and simpler lower order approaches. In particular, our method allows to retain important discrete conservation properties, that to the best of our knowledge have never been proven for high order finite element approaches, while maintaining the simplicity of the  $RT_0$ , that also enables the use of very efficient semi-implicit discretizations such as those proposed in [6]. Furthermore, semi-Lagrangian techniques such as those proposed in [8, 23] can benefit of the proposed reconstruction technique by effectively reducing the amount of numerical diffusion introduced by the interpolation step.

#### ACKNOWLEDGEMENTS

The authors were partly supported by the Max-Planck Institute for Meteorology, Hamburg, through the ICON project. Special thanks go to J. Baudisch, who has provided first preliminary results through his Master Thesis [2]. Many useful conversations with W. Sawyer on the application of radial kernels in computational fluid dynamics are gratefully acknowledged, as well as earlier contributions by T. Heinze and L. Kornblueh to the development of the ICON shallow water model.

#### REFERENCES

1. A. Arakawa and V. Lamb. A potential enstrophy and energy conserving scheme for the shallow water equations. *Monthly Weather Review*, 109:18–136, 1981.
2. J. Baudisch. Accurate Reconstruction of Vector Fields Using Radial Basis Functions. Master's thesis, Munich University of Technology, Germany, 2005.
3. J. Behrens and A. Iske. Grid-free adaptive semi-Lagrangian advection using radial basis functions. *Comput. Appl. Math.*, 43:319–327, 2002.
4. J. Behrens, A. Iske, and M. Käser. Adaptive meshfree method of backward characteristics for nonlinear transport equations. In *Meshfree Methods for Partial Differential Equations*, pages 21–36, Berlin, 2002. Springer.
5. L. Bonaventura, L. Kornblueh, T. Heinze, and P. Ripodas. A semi-implicit method conserving mass and potential vorticity for the shallow water equations on the sphere. *Intern. J. Numer. Methods Fluids*, 47:863–869, 2005.
6. L. Bonaventura and T. Ringler. Analysis of discrete shallow water models on geodesic Delaunay grids with C-type staggering. *Monthly Weather Review*, 133:2351–2373, 2005.
7. M. D. Buhmann. *Radial Basis Functions*. Cambridge University Press, Cambridge, UK, 2003.
8. V. Casulli and R. A. Walters. An unstructured grid, three-dimensional model based on the shallow water equations. *Intern. J. Numer. Methods Fluids*, 32:331–348, 2000.
9. C. Franke and R. Schaback. Convergence order estimates of meshless collocation methods using radial basis functions. *Adv. Comput. Math.*, 8:381–399, 1998.
10. C. Franke and R. Schaback. Solving partial differential equations by collocation using radial basis functions. *Appl. Math. Comput.*, 93:73–82, 1998.
11. M. Griebel and M. A. Schweitzer, editors. *Meshfree Methods for Partial Differential Equations*, volume 26 of *Lecture Notes in Computational Science and Engineering*, Berlin, 2002. Springer.
12. M. Griebel and M. A. Schweitzer, editors. *Meshfree Methods for Partial Differential Equations II*, volume 43 of *Lecture Notes in Computational Science and Engineering*, Berlin, 2005. Springer.
13. M. Griebel and M. A. Schweitzer, editors. *Meshfree Methods for Partial Differential Equations III*, volume 57 of *Lecture Notes in Computational Science and Engineering*, Berlin, 2006. Springer.
14. M. Griebel and M. A. Schweitzer, editors. *Meshfree Methods for Partial Differential Equations IV*, volume 65 of *Lecture Notes in Computational Science and Engineering*, Berlin, 2008. Springer.
15. F. Hermeline. Two coupled particle-finite volume methods using Delaunay-Voronoi meshes for the approximation of Vlasov-Poisson and Vlasov-Maxwell equations. *J. Comput. Phys.*, 106:1–18, 1993.

16. A. Iske. Reconstruction of functions from generalized Hermite-Birkhoff data. In *Approximation Theory VIII. Vol. 1: Approximation and Interpolation*, pages 257–264, Singapore, 1995. World Scientific.
17. A. Iske. *Multiresolution Methods in Scattered Data Modelling*. Springer, Berlin, 2004.
18. A. Iske. Particle flow simulation by using polyharmonic splines. In *Algorithms for Approximation*, pages 83–102, Berlin, 2007. Springer.
19. A. Iske and T. Sonar. On the structure of function spaces in optimal recovery of point functionals for ENO-schemes by radial basis functions. *Numer. Math.*, 74:177–202, 1996.
20. M. Käser and A. Iske. ADER schemes on adaptive triangular meshes for scalar conservation laws. *J. Comput. Phys.*, 205:486–508, 2005.
21. P. Khurd, R. Verma, and C Davatzikos. Kernel-based manifold learning for statistical analysis of diffusion tensor images. In *Information Processing in Medical Imaging*, pages 581–593, Berlin, 2008. Springer.
22. C. A. Micchelli. Interpolation of scattered data: distance matrices and conditionally positive definite functions. *Constr. Approx.*, 2:11–22, 1986.
23. E. Miglio, A. Quarteroni, and F. Saleri. Finite element approximation of quasi-3d shallow water equations. *Computational Methods in Applied Mechanics and Engineering*, 174:355–369, 1999.
24. F. J. Narcowich and J. D. Ward. Generalized Hermite interpolation via matrix-valued conditionally positive definite functions. *Math. Comp.*, 63:661–687, 10 1994.
25. J.C. Nedélec. Mixed finite elements in  $\mathbf{R}^3$ . *Numer. Math.*, 35:315–341, 1980.
26. J. Pedlosky. *Geophysical Fluid Dynamics*. Springer, New York, 1987.
27. B. Perot. Conservation properties of unstructured staggered mesh schemes. *J. Comput. Phys.*, 159:58–89, 2000.
28. A. Quarteroni and A. Valli. *Numerical Approximation of Partial Differential Equations*. Springer, Berlin-Heidelberg, 1994.
29. D. A. Randall. Geostrophic adjustment and the finite-difference shallow water equations. *Monthly Weather Review*, 122:1371–1377, 1994.
30. P. A. Raviart and J. M. Thomas. A mixed finite element method for 2nd order elliptic problems. In *Mathematical aspects of finite element methods*, pages 292–315. Springer, 1977.
31. T.D. Ringler and D.A. Randall. A potential enstrophy and energy conserving numerical scheme for solution of the shallow-water equations a geodesic grid. *Monthly Weather Review*, 130:1397–1410, July 2002.
32. G. Rosatti, L. Bonaventura, and D. Cesari. Semi-implicit, semi-Lagrangian environmental modelling on Cartesian grids with cut cells. *J. Comput. Phys.*, 204:353–377, 2005.
33. G. Rosatti, L. Bonaventura, and R. Chemotti. High order interpolation methods for semi-Lagrangian models of mobile-bed river hydrodynamics on Cartesian grids with cut cells. *Intern. J. Numer. Methods Fluids*, 47:863–869, 2005.
34. D. Y. Le Roux, C. A. Lin, and A. Staniforth. An accurate interpolating scheme for semi-Lagrangian advection on an unstructured grid for ocean modelling. *Tellus A*, 49A:119–138, 1997.
35. R. Schaback. Error estimates and condition numbers for radial basis function interpolation. *Adv. Comput. Math.*, 3:251–264, 1995.
36. R. Schaback and H. Wendland. Kernel techniques: from machine learning to meshless methods. *Acta Numerica*, pages 543–639, 2006.
37. M. Shashkov, B. Swartz, and B. Wendroff. Local reconstruction of a vector field from its normal components on the faces of grid cells. *J. Comput. Phys.*, 139:406–409, 1998.
38. T. Sonar. Optimal recovery using thin plate splines in finite volume methods for the numerical solution of hyperbolic conservation laws. *IMA J. Numer. Anal.*, 16:549–581, 1996.
39. H. Wendland. Meshless Galerkin methods using radial basis functions. *Math. Comp.*, 68:1521–1531, 1999.
40. H. Wendland. *Scattered Data Approximation*. Cambridge University Press, Cambridge, UK, 2005.
41. D. L. Williamson, J. B. Drake, J. J. Hack, R. Jakob, and P. N. Swarztrauber. A standard test set for numerical approximations to the shallow water equations in spherical geometry. *J. Comput. Phys.*, 102:211–224, 1992.
42. S. M. Wong, Y. C. Hon, and M. A. Golberg. Compactly supported radial basis functions for shallow water equations. *Appl. Math. Comp.*, 127:79–101, 2002.